Optimal method for exoplanet detection by spectral and angular differential imaging

A. Cornia[a,b], L. M. Mugnier[a], D. Mouillet[c], A. Vigan[d], A. Eggenberger[c], G. Rousset[b], A. Boccaletti[b], M. Carbillet[e], K. Dohlen[d], T. Fusco[a], J. Carson[f], and G. Montagnier[g].

[a] ONERA/DOTA, B.P. 72, 92322 Châtillon cedex, France.
[b] LESIA, Observatoire de Paris, 5 place Jules Janssen, 92195 Meudon, France.
[c] Lab. d'Astrophysique de l'Observatoire de Grenoble, France.
[d] Observatoire Astronomique de Marseille-Provence, France.
[e] Université de Nice Sophia Antipolis, France.
[f] MPIA, Heidelberg, Germany.
[g] ESO, Paranal, Chile.

ABSTRACT

In the context of the SPHERE planet finder project, we further develop and characterize a recently proposed method for the efficient direct detection of exoplanets from the ground using spectral and angular differential imaging. The method, called ANDROMEDA, combines images appropriately into "pseudo-data", then uses all of them in a Maximum-Likelihood framework to estimate the position and flux of potential planets orbiting the observed star. The method is validated on realistic simulations of images performed by the SPHERE consortium, and applied to experimental data taken by the VLT/NAOS-CONICA instrument.

Keywords: exoplanets, detection, inverse problems, coronagraphy, angular imaging, differential imaging, spectral imaging, high contrast, maximum likelihood, adaptive optics.

1. INTRODUCTION

The direct detection of exoplanets from the ground is a very promising field of astronomy today. A goal is the characterization of the physical composition of the exoplanets by a spectral analysis of their emitted and/or reflected light. This observation from the ground is a technological challenge. Indeed, in order to be able to observe a sufficient number of targets, it is required to cope with an intensity ratio (also called contrast) between the star and its planet that may be as high as 10^6 in IR bands at very small angular separations. In particular, our work is focused on the SPHERE project.[1] This instrument, which will be mounted on VLT of ESO in 2011, is the combination between several optical features, all of them optimized toward the final goal, which is exoplanet detection. First of all, the extreme adaptive optics system (XAO) concentrates the light into a coherent Airy pattern, performing a real-time correction of atmospheric turbulence.[2] Then, the coronagraphic stage[3–5] strongly attenuates the star intensity and therefore significantly reduces the photon noise.

Furthermore, in order to reach the detection performance needed to detect a large number of planets, it is mandatory to combine the above-mentioned optical devices to an a posteriori processing of all the data. The main issue is to disentangle the potential planet signal from the quasi-static speckles, which are due to static aberrations and constitute a major "noise" source. These speckles present the same characteristic angular size as the planet signal, λ/D. To enhance the capability to discriminate between the speckles and the planet, SPHERE observes simultaneously in different spectral channels with an integral field spectrograph or with a dual band imager (IRDIS): by subtracting the two images taken simultaneously at different wavelengths, it is possible to eliminate most of residual aberrations.[7] The two wavelengths are chosen in such a way that there is a strong contrast between the planet fluxes at each of them. But yet, this is not sufficient: one needs to develop a sophisticated method of images processing which allows to exploit also the temporal information. On SPHERE, the pupil is stabilized during the night in order to keep the aberrations fixed, while the field rotates, thus making

Further author information: send correspondence to A. Cornia: alberto (dot) cornia (at) onera (dot) fr

easier to distinguish the aberration-induced speckles from the planet(s). If the static aberrations are not known, but vary slowly during the night, it is possible to eliminate their influence via appropriate subtractions between images taken at different instants. This is the principle of the Angular Differential Imaging (ADI).[8,9] These double (spectral+angular) differences are the data on which our method is to be applied.

Here we present further developments of ANDROMEDA, the method proposed in Mugnier et al. (2009).[10] Like other methods of planet detection,[9,11] ANDROMEDA's aim is to subtract as well as possible the star signal. But one specific feature of our method is that it performs a characterization (detection and flux estimation) founded on a sound statistical basis in a Maximum-Likelihood framework.

After having recalled the principle of the method in Sect. 2, in Sect. 3 we present in detail the pre-processing of ANDROMEDA, which allows us to exploit the spectral information present in the data, and relies on an optimization of the spectral and angular differences. In Sect. 4 we show the results of tests of ANDROMEDA on simulated data reproducing realistic conditions of observation. Then in Sect. 5 we will present the results of its application on experimental data taken by the VLT.

2. PRINCIPLE OF THE ANDROMEDA METHOD

The basis of the method lies on Angular Differential Imaging. The IRDIS instrument, which is a part of SPHERE, allows to de-rotate the pupil during the observation, so that the speckle pattern stays almost constant while the field (and the planet(s) within it) rotates around the center during the night. We can thus strongly reduce the influence of the speckles via appropriated subtractions between images taken at two different instants: in the difference, the star signal is suppressed as much as possible and only the planet signal and the noise are left. An example of a differential image is shown in Fig. 1, on the right.

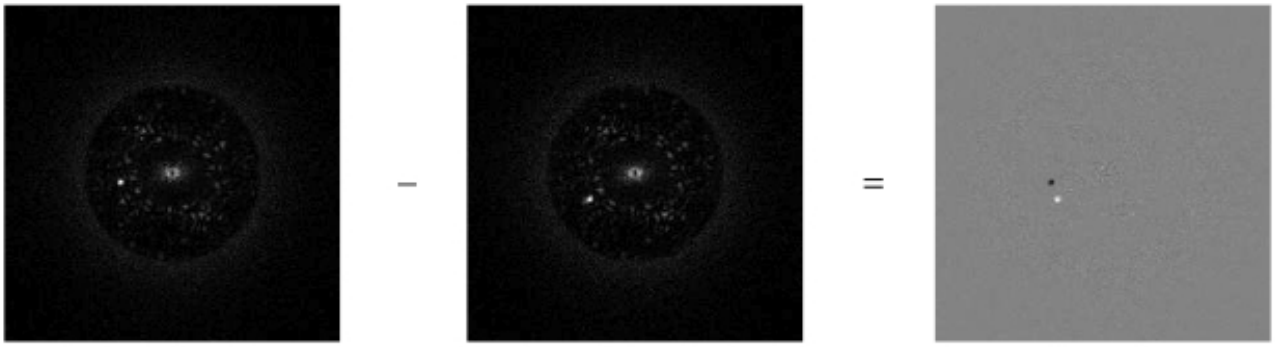

Figure 1. Example of an angular difference. We can remark the two peaks (one positive, one negative) corresponding to the position of the planet at the two instants, and the residual noise.

The new data consist of a set of differential images denoted by $\Delta(\boldsymbol{r}, k)$; $\boldsymbol{r}$ is the position of the pixel, and k is an index associated with each couple of images to be subtracted (that is to say, the k-th differential image is the difference between two images taken at instants $t_1(k)$ and $t_2(k)$: $\Delta(\boldsymbol{r}, k) = i_{t_1(k)} - i_{t_2(k)}$). Assuming that the star has been suppressed, the model for $\Delta(\boldsymbol{r}, k)$ can be written as:

$$\Delta(\boldsymbol{r}, k) = a \cdot \boldsymbol{p}(\boldsymbol{r}, k; \boldsymbol{r}_0) + \boldsymbol{n}(\boldsymbol{r}, k), \tag{1}$$

where a is the planet's flux and $\boldsymbol{r}_0$ is the initial planet's position, $\boldsymbol{p}(\boldsymbol{r}, k; \boldsymbol{r}_0)$ is the known "planet signature" in this data for an assumed $\boldsymbol{r}_0$ (it is the difference of two PSF's), and $\boldsymbol{n}(\boldsymbol{r}, k)$ denotes the noise.

The maximum likelihood approach consists in searching for $(\hat{\boldsymbol{r}}_0, \hat{a})$ that maximize the likelihood. We define a criterion $J(\boldsymbol{r}_0, a)$ which is equal to the logarithm of the likelihood up to an unimportant constant. In the following we assume that the noise has a variance $\sigma^2(\boldsymbol{r}, k)$, which can be estimated from the cube of images.

The log-likelihood is given by:

$$J(\boldsymbol{r}_0, a) = \ln L(\boldsymbol{r}_0, a) = -\sum_{\boldsymbol{r},k} \frac{|\Delta(\boldsymbol{r},k) - a \cdot p(\boldsymbol{r},k;\boldsymbol{r}_0)|^2}{2\sigma^2(\boldsymbol{r},k)}. \tag{2}$$

Incidentally, maximizing the likelihood is equivalent to minimizing the sum of the squared residuals between data Δ and model $a \cdot p$, weighted by the noise variance.

The expression of the log-likelihood is quadratic with respect to a, so the optimal value $\hat{a}(\boldsymbol{r}_0)$ of a for each given $\boldsymbol{r}_0$ is computable analytically:

$$\hat{a}(\boldsymbol{r}_0) = \frac{\sum_{\boldsymbol{r},k} p(\boldsymbol{r},k;\boldsymbol{r}_0)\Delta(\boldsymbol{r},k)/\sigma^2(\boldsymbol{r},k)}{\sum_{\boldsymbol{r},k} p^2(\boldsymbol{r},k;\boldsymbol{r}_0)/\sigma^2(\boldsymbol{r},k)} \tag{3}$$

It can be pointed out that $\hat{a}(\boldsymbol{r}_0)$ is a weighted cross-correlation between the planet signature p and the signal Δ.

If we insert this optimal value for the flux into the metric J, we obtain an expression of the latter that depends, explicitly at least, only on the sought planet position:

$$J'(\boldsymbol{r}_0) \triangleq J(\boldsymbol{r}_0, \hat{a}(\boldsymbol{r}_0)) = \frac{\left(\sum_{\boldsymbol{r},k} p(\boldsymbol{r},k;\boldsymbol{r}_0)\Delta(\boldsymbol{r},k)/\sigma^2(\boldsymbol{r},k)\right)^2}{\sum_{\boldsymbol{r},k} p^2(\boldsymbol{r},k;\boldsymbol{r}_0)/\sigma^2(\boldsymbol{r},k)}. \tag{4}$$

This criterion J' can be computed for each possible initial planet position on a grid, which can be chosen as the original pixel grid of the images, or as a finer grid if it is useful. The most likely initial planet's position is then $\hat{\boldsymbol{r}}_0 = \arg\max J'(\boldsymbol{r}_0)$, and the most likely flux is $\hat{a}(\hat{\boldsymbol{r}}_0)$ as computed with Eq. 3.

The typical shapes of the $\hat{a}(\boldsymbol{r}_0)$ and $J'(\boldsymbol{r}_0)$ maps are shown in Fig. 2. In the former we can see the central positive peak with two negative sidelobes; in the latter there are still two sidelobes, but they are positive and lower than the central peak, which represents the most probable position of the planet.

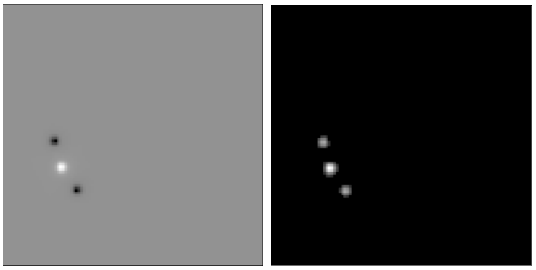

Figure 2. Example of estimated flux map $\hat{a}(\boldsymbol{r}_0)$ and likelikood map $J'(\boldsymbol{r}_0)$, for a noiseless case.

We can also define the standard deviation on estimated flux $\sigma(\hat{a}(\hat{\boldsymbol{r}}_0))$, which reflects the noise propagation from data to the computed flux map. It can be shown[10] that

$$\sigma(\hat{a}(\boldsymbol{r}_0)) = \left(\sum_{\boldsymbol{r},k} \frac{p^2(\boldsymbol{r},k;\boldsymbol{r}_0)}{\sigma^2(\boldsymbol{r},k)}\right)^{-\frac{1}{2}}. \tag{5}$$

So we can define also the signal-to-noise ratio as the estimated flux divided by its standard deviation:

$$\mathrm{SNR}(\boldsymbol{r}_0) = \frac{\hat{a}(\boldsymbol{r}_0)}{\sigma(\hat{a}(\boldsymbol{r}_0))} = \frac{\sum_{\boldsymbol{r},k} p(\boldsymbol{r},k;\boldsymbol{r}_0)\Delta(\boldsymbol{r},k)/\sigma^2(\boldsymbol{r},k)}{\sqrt{\sum_{\boldsymbol{r},k} p^2(\boldsymbol{r},k;\boldsymbol{r}_0)/\sigma^2(\boldsymbol{r},k)}} \tag{6}$$

Incidentally, it can be pointed out that $(\mathrm{SNR}(\boldsymbol{r}_0))^2 = J'(\boldsymbol{r}_0)$, which means that the most likely position for a planet is the one for which the SNR is the highest. Indeed, maximizing the two quantities is equivalent. The most likely planet position is thus the value $\hat{\boldsymbol{r}_0}$ of $\boldsymbol{r}_0$ that maximizes $\mathrm{SNR}(\boldsymbol{r}_0)$, and the estimated flux is the value at the same position of the flux map, $\hat{a}(\hat{\boldsymbol{r}_0})$.

This estimator can be improved by constraining the estimated flux to be positive. Indeed, the value of $\hat{a}(\boldsymbol{r}_0)$ of Eq. 3 is not necessarily positive, whereas the true flux is. So we can threshold the flux map to the positive values only; this is equivalent to thresholding the SNR map, since the two quantities have the same sign. And since $(\mathrm{SNR}(\boldsymbol{r}_0))^2 = J'(\boldsymbol{r}_0)$, this thresholding leads to the disappearance of some spurious peaks in the likelihood map.[10] In particular, the positivity constraint cancels the two sidelobes both in the flux map and in the likelihood map shown in Fig. 2.

The detection criterion proposed in Mugnier et al. (2009)[10] is based on the Gaussianity and the whiteness of the noise, a hypothesis which is strictly fulfilled if we have only photon and detector noise (i.e., if the PSF of the star does not vary through the night). This criterion consists in deciding that a planet is present in $\boldsymbol{r}_0$ iff $\mathrm{SNR}(\boldsymbol{r}_0)$ is greater than a certain threshold τ. The Probability of False Alarm (PFA) is linked to this threshold by the relationship $\mathrm{PFA}(\tau) = 1 - \mathrm{erf}(\tau)$, where $\mathrm{erf}(x) = \frac{1}{\sqrt{2\pi\sigma^2}} \int_{-\infty}^{x} \exp\left(-\frac{(x'-\mu)^2}{2\sigma^2}\right) dx'$.

3. PRE-PROCESSING: OPTIMAL SUPPRESSION OF THE SPECKLES

ANDROMEDA uses differential images in which the star signal is supposed to have been suppressed as well as possible. This suppression can be made in two complementary ways:

- by spectral difference of images taken at the same instant (SDI, for Spectral Differential Imaging);
- by difference of two images taken in the same spectral channels at two different instants, with a sufficient field rotation between the two (ADI, for Angular Differential Imaging).

In this section we explain how to perform these operations in the optimal way.

3.1 Principle of the spectral differentiation

The IRDIS instrument allows to work in dual band imaging mode, which means that images can be taken simultaneously at two different wavelengths, λ_1 and λ_2. This can help us eliminate the speckles more effectively, via an appropriate spectral subtraction. To do so, the spectral channels must be chosen in such a way that the speckle pattern does not change too much between them (so they must be as close as possible[6,7]), but at the same time there must be a significant difference in the planet flux at the two wavelengths, to avoid that the planet signal is cancelled in the difference. This happens if, for example, we have an absorption line in the spectrum of the planet at one of the two wavelengths. In the following we make the assumption that the planet flux at λ_2 is negligible.

Prior to performing the spectral differences, a rescaling of the images taken in one of the two channels (at λ_2, if the planet is absent at this wavelength) must be carried out, because the shape and amplitude of the PSF varies according to the wavelength.

Assuming that we use an extreme AO system, a perfect coronagraph, that aberrations are achromatic, and that the small phase approximation is valid, a coronagraphic star image at λ_i, denoted by $h_i^c(\alpha)$, scales spatially proportionally to λ_i, so that:

$$h_2^c\left(\frac{\lambda_2}{\lambda_1}\boldsymbol{r}\right) = \left(\frac{\lambda_1}{\lambda_2}\right)^2 h_1^c(\boldsymbol{r}) \tag{7}$$

So i_2 must be scaled according to Eq. 7: the image to be subtracted to i_1 is given by

$$i_{2,res}(\boldsymbol{r}) = \left(\frac{\lambda_2}{\lambda_1}\right)^2 i_2\left(\frac{\lambda_2}{\lambda_1}\boldsymbol{r}\right) \tag{8}$$

Because SPHERE images are at least Shannon-sampled, this scaling can be done accurately using the discrete Fourier transform (DFT) – in practice the FFT. In a nutshell, our scaling method consists in zero-padding the image both in direct space and in Fourier space in order to obtain the zoom factor of our choice. The exact steps are detailed in appendix A.

3.2 Principle of the angular differentiation: choice of the image pairs

For each of the original images, we construct a differential image Δ_k by subtracting another image from it, chosen so that the field has sufficiently rotated in the meantime. In case spectral differences are performed (as described in Subsect. 3.1), they can be used instead of the original images to build up angular differences.

On the one hand we want to subtract images as close as possible in time, so that the speckles have not evolved significantly from one image to the other. On the other hand we must pay attention not to take two images too close, because if the planet has moved too little between the two images its signal is cancelled out, leaving only noise in the differential image.

So it is important to set the minimum acceptable separation δ_{min} between the positions of the planet in the two images: larger values of δ_{min} will result in a less effective quasi-static speckle subtraction; smaller values will cause a more important flux loss. The best compromise between these two effects depends on the speckle evolution time, i.e., on the instrument's stability.

δ_{min} is expressed in units of length (λ/D, pixels or arcseconds; we generally use the first one to make the flux loss independent of the wavelength). Once δ_{min} is set, the minimum acceptable angle θ_{min} by which the field has rotated between the two images depends on the distance ρ from the rotation center, according to the formula $\theta_{min}(\rho) = 2\arcsin(\delta_{min}/2\rho)$. θ_{min} is a decreasing function of ρ, which means that when we are farther from the star we are allowed to take images closer in time.

It should be noted that the choice of δ_{min} does not affect the flux estimation (contrarily to what happens for example with LOCI[11]), because the overlapping of the planet signals in differential images is taken into account in the shape of the planet signature $p(\boldsymbol{r}, k; \boldsymbol{r}_0)$.

3.3 Optimization of differences

When performing a difference (spectral or angular) between two images i_1 and i_2 we cannot simply take the value $i_1 - i_2$, because the two images will have different fluxes in the two channels. Thus we have to multiply the second image by a certain factor, which we will call γ. The optimized spectral and angular differences can be written, respectively, as:

$$i'_t = i_t^{\lambda_1} - \gamma_t i_{t,res}^{\lambda_2}, \tag{9}$$

$$\Delta_k = i'_{t_1(k)} - \gamma'_k i'_{t_2(k)}, \tag{10}$$

where $i_t^{\lambda_j}$ is the image taken at the instant t at the wavelength λ_j; $i_{t,res}^{\lambda_2}(\boldsymbol{r}) = \left(\frac{\lambda_2}{\lambda_1}\right)^2 i_t^{\lambda_2}\left(\frac{\lambda_2}{\lambda_1}\boldsymbol{r}\right)$ according to Eq. 8; $t_1(k)$ and $t_2(k)$ are the two instants at which the images used to build the k-th differential image are taken. For the spectral difference, the flux variation is due to the fact that the star spectrum is not perfectly flat around the two considered wavelengths and to the difference in the transmission factor between the two channels; the flux variation in time is essentially caused by the difference in the quality of AO correction during the night.

Furthermore, we have noticed both on simulated and experimental images that this variation depends greatly on the distance to the center. As a consequence, we shall split the zone in which we want to detect planets in several concentric annuli and perform the optimizations of differences separately on each of these annuli. We will refer to each annulus as the "subtraction area".*

To explain how to obtain the coefficients γ_t and γ'_k, for simplicity we will now write the differences in Eqs. 9 and 10 in the generic form $|i_1 - \gamma i_2|^2$; the procedure is the same for both cases.

*It can be noticed that the idea of an optimization that depends on the considered position in the image is common to other methods of planet detection, such as "smart" ADI[9] and LOCI.[11]

For each subtraction area, the coefficients γ is computed as the one that minimizes the total of the squared difference $|i_1 - \gamma i_2|^2$, restricted to a certain area, which we will call the "optimization area". It can be shown that

$$\gamma = \frac{\sum_{\boldsymbol{r}} m(\boldsymbol{r}) \cdot i_1(\boldsymbol{r}) \cdot i_2(\boldsymbol{r})}{\sum_{\boldsymbol{r}} m(\boldsymbol{r}) \cdot i_2^2(\boldsymbol{r})}, \tag{11}$$

where m is a mask that is equal to 1 on the pixels belonging to the optimization area, and 0 elsewhere. In principle we could take the optimization areas equal to the subtraction areas. In practice, if we choose this solution, we observe that there are evident discontinuities both in the SNR map and in the flux map corresponding to the limits of the annuli. To overcome this problem, we choose an optimization area larger than the subtraction area. Each optimization area is an annulus which shares the same inner radius as the subtraction area but has a larger outer radius.[11] The ratio between these two areas is constant for all the annuli and is an input of the algorithm; we will refer to it as R_A. The main advantage of having an optimization area larger than the subtraction area is that the optimization areas for consecutive annuli overlap, causing a smoothing of the discontinuities, as we will see later (Sect. 5).

4. TEST OF ANDROMEDA ON SIMULATED REALISTIC DATA

4.1 Simulation conditions

The method has been tested on data elaborated simulating SPHERE performances. The simulations were aimed at reproducing observation conditions as realistically as possible. These conditions are the same listed in Vigan et al. (2010)[12] and in the article of Vigan et al. for this conference.[13]

We have 144 images taken during one night, for a total exposure time of 4 hours (that is to say 100 s per image). We take into account the variation of quality of AO correction (using 100 different phase screens for each image) due to the variation of the seeing ($0.85'' \pm 0.15''$) and of the wind speed, the quasi-static aberrations caused by the elements of the optics and their change of positions during the night. The achromatic pre-coronagraph RMS wavefront error varies between 29.2 and 30.1 nm. We work at wavelengths $\lambda_1 = 1.587$ and $\lambda_2 = 1.667$ µm (the former is the one at which the planet flux is much higher, because at λ_2 there is a deep absorption line of methane). Noise is a mixture of photon and detector noise.

In the simulated data there are four rows of six planets each, of equal flux, placed at 90° from each other; the planets are at separations of $0.2''$, $0.5''$, $1''$, $1.5''$, $2''$ and $2.5''$. In units of λ/D, these distances correspond to 4.9, 12.2, 24.3, 36.5, 48.7 and 60.9 for λ_1. We are considering a G0 star at a distance of 10 pc. The flux rate on the pupil plane is $2.67 \cdot 10^7$ phot/s/m^2; for the chosen exposure time, and taking into account the transmission factor and the coronagraphic attenuation, the mean number of photon in each image is $1.69 \cdot 10^9$. We have simulated two different sets of data with two levels of star/planet contrast, to test ANDROMEDA both when performing angular differences only (contrast: $7.5 \cdot 10^4$) and when performing spectral+angular differences (contrast: 10^6). Furthermore, we neglect the field rotation within one exposure (which causes a slight smearing of the planetary signal).

4.2 Detection parameters

4.2.1 Definition of the detection area

The computing time of ANDROMEDA is roughly proportional to the number of positions on which we want to detect a planet (which correspond to the pixel grid of the images) and to the number of images. So it is of interest to limit the area on which we want to use it, in order to keep the processing time reasonable.

Since ANDROMEDA's principle consists in removing as much as possible the star speckles, we expect it to be more useful where the speckle noise dominates, i.e. at small separations from the star. To determine the maximum radius at which we want to use ANDROMEDA, we compare its performance to that of a simpler method, which consists in simply de-rotating every image according to its parallactic angle and sum up the results, then subtracting the azimuthal median for each distance.

In Fig. 3, we see that the three outer planets are clearly detectable with both methods, while only ANDROMEDA can detect the three inner ones. Indeed we can see that in the sum of the de-rotated images there

are still too many residuals of the speckles not only inside the AO correction halo, which is at a distance of $20\lambda/D$ (as expected, since the deformable mirror has 40×40 actuators), but also in a region which extends further, up to a distance of about $30\lambda/D$ from the center. So this has been set as the standard radius of the detection area. It is equal to 100 pixels at 1.65 µm, which corresponds to about 30000 tested positions. The limit of the detection area falls between the third and fourth planet of each row; this is why in the results presented we are expected to see only three planets per row (the field of view is restricted with respect to the images shown in Fig. 3).

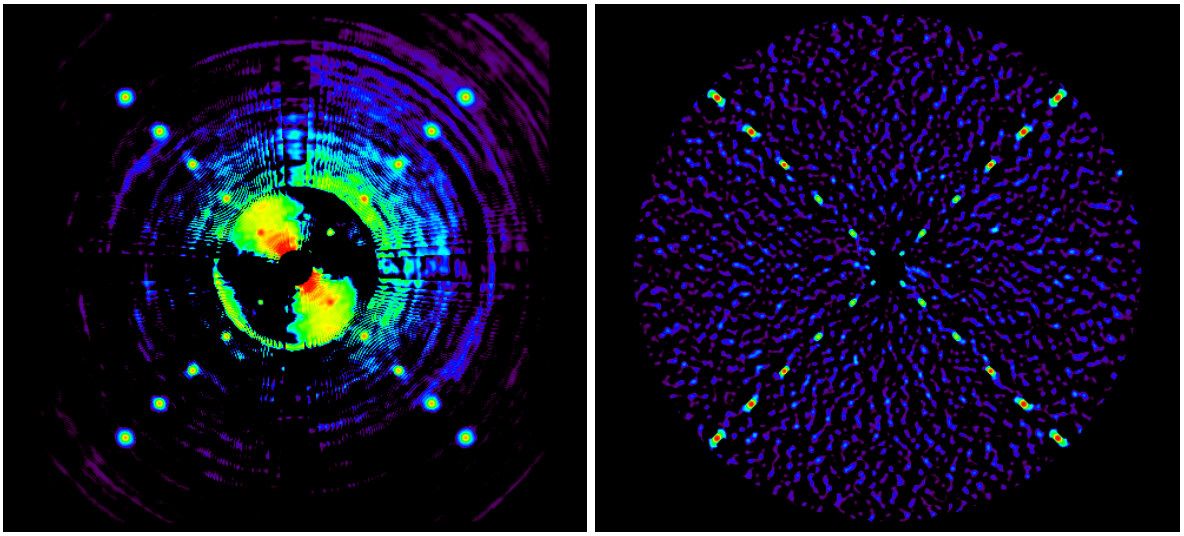

Figure 3. Comparison between a simple ADI method (left, see text) and the SNR map obtained with ANDROMEDA (right). The field of view of the area is $5''$.

4.2.2 Parameters used for the detection and computing time

The parameters used as inputs for the reconstruction with ANDROMEDA are the following:

- inner radius of the detection area: $4\lambda/D$;
- outer radius of the detection area: $30\lambda/D$;
- PSF used for the reconstruction: array of 32×32 pixels;
- $\delta_{min} = 1\lambda/D$;
- thickness of the subtraction annuli: 1 pixel;
- $R_A = 30$, i.e., each optimization annulus is 30 times larger than the related subtraction annulus;
- image noise variance estimated empirically from the cube of images (we take a variance map constant in time, equal to the variance in time computed on each pixel).

To give an idea of the computing time, on a MacBook Pro with a 2.2 GHz Intel Core 2 Duo processor ANDROMEDA takes about 5 minutes to yield a detection map for this area in the simulation conditions given above (144 images). In reality we expect to have a greater number of images (~ 1000), so this computing time would be multiplied by less than a factor 10, staying into reasonable limits.

4.3 Effect of the speckle noise on the SNR map

At the end of Sect. 2 we defined the signal-to-noise ratio as the ratio between the estimated flux and its estimated standard deviation. If the noise is white and gaussian, we expect the standard deviation of the values of the SNR map to be around 1 (excluding the points where we have detections); the threshold represent the number of σ's of confidence for which we have a detection. Typically, when photon noise only is present we detect all planets at a threshold of $\sim$3-4.[10] If the standard deviation in the SNR map is not 1, which happens typically in presence of speckle noise (as we will see in Subsect. 4.4 and 4.5), this map must be normalized in order to get the correct values for the threshold. We think that the higher value of the SNR standard deviation in the presence of speckle noise is due to the fact that this source of noise is not white, i.e., there is an important time correlation of the speckle noise between the images.

4.4 Angular Differential Imaging only

Fig. 4-a shows the SNR map that we obtain when we perform angular differences only on a cube of images for which the star/planet contrast is $7.5 \cdot 10^4$. Fig. 4-b shows a thresholded version of the same map at a value of 3, which means that planets are detected at 3σ.[†]

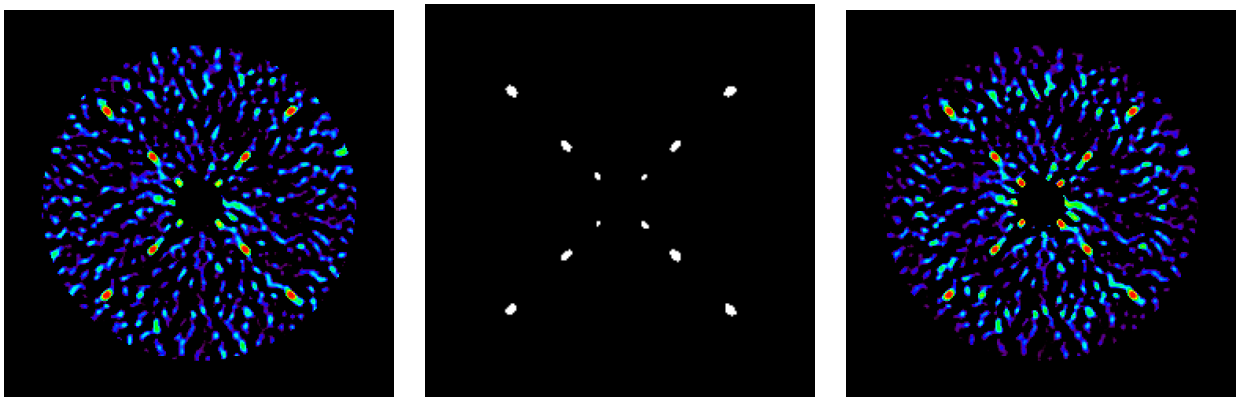

(a) (b) (c)

Figure 4. SNR map for ADI (a), its thresholded version at 3 (b) and the related flux map (c). The star/planet flux contrast is $7.5 \cdot 10^4$.

From the thresholded map we can see that the four planets closest to the star (at $0.2''$) are more difficult to detect than the other ones (their peaks are lower). This is easily understandable because the speckle and photon noise towards the center is much higher, and also because the movement of the planet due to the field rotation is smaller, making the discrimination of it against the speckles more difficult.

Incidentally, on the SNR map we can see that the peaks corresponding to the planets have an elongated shape in the radial direction. This happens because, if we choose a small value for the angular separation between the images chosen to build the angular differences, the two negative sidelobes in the flux map (see Fig. 2) get closer to the central peak and overlap it to a greater extent. The central peak is thus partially cancelled in the tangential direction. This shape is a sort of trace of the presence of a planet which can be used to recognize more easily real detections of point sources in the presence of instrumental and/or reduction artifacts.

If we look at the estimated flux map (Fig. 4-c) we see that it has a different appearance with respect to the SNR map. Indeed the height of the peaks related to the planets at $0.2''$ is comparable to the one of the other planets, as expected, since the planets all have the same flux in these simulations. The error on the estimated flux is somewhat large for the innermost planets (between 20% and 40%), once again due to the influence of the noise. The error for all the other planets is below 4%.

[†]The standard deviation of the values of the SNR was 6.25 before normalization.

4.5 Spectral+Angular Differential Imaging

We show here the results of ANDROMEDA when we perform both spectral and angular differences; the contrast is now 10^6. As in the previous case, we present in Fig. 5-a the SNR map and in Fig. 5-b its thresholded version at 3.[‡] In this case, too, the innermost planets are less easily detectable.

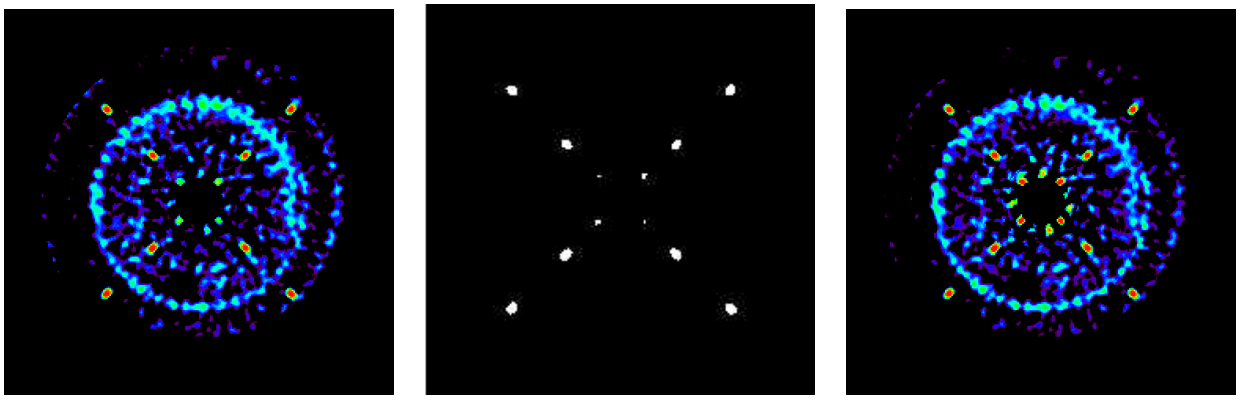

(a) (b) (c)

Figure 5. SNR map for SDI+ADI (a), its thresholded version at 3 (b) and the related flux map (c). The star/planet flux contrast is 10^6.

Again, the flux map (Fig. 5-c) shows central peaks roughly of the same height as the others. The errors on the estimated flux for the inner planets are lower than the ones of Subsect. 4.4 (between 10% and 16%). The error for the other planets is below 6%.

5. APPLICATION OF ANDROMEDA TO EXPERIMENTAL DATA

As a further preparatory step towards the analysis of SPHERE data, we now run ANDROMEDA on VLT/NACO images taken in pupil tracking mode (ADI) in the H band (1.65 µm). These data are collected in the context of an ongoing large program (PI J.-L. Beuzit) aimed at probing the occurrence of exoplanets and brown dwarfs at wide separations (5-500 AU).

We present here the results obtained for a target observed in saturated imaging for a total exposure time of 1.8 hour (319 images of 6.8-s integration time each). The magnitude of the star is $V = 9.25$. The seeing is $0.81'' \pm 0.14''$. A quick-look analysis performed with simple ADI revealed the presence of a large number of faint point-like sources surrounding the star. Although these companion candidates are very likely background stars, from a detection perspective they are good proxies for true substellar companions.

The detection parameters used in the reconstruction with ANDROMEDA are the following:

- inner radius of the detection area: $28\lambda/D$ (120 pixels; we did not consider a large portion around the center to avoid the zone of saturation);
- outer radius of the detection area: $145\lambda/D$ (480 pixels);
- PSF used for the reconstruction: array of 32×32 pixels;
- $\delta_{min} = 1\lambda/D$;
- thickness of the subtraction annuli: 24 pixels;
- $R_A = 1$ and 3;

[‡]In this case the standard deviation of the SNR map before normalization is lower (4.71), because of the most effective elimination of the speckles through the spectral differences.

- image noise variance estimated empirically as for the simulated images.

With respect to the tests on simulated data, this time we took smaller values for R_A and larger values for the thickness of annuli. This has been done to show more clearly the influence of R_A on the quality of detection, as discussed in Subsect. 3.3. On the left of Fig. 6 we show the SNR map obtained taking $R_A = 1$ (so that optimization areas are equal to subtraction areas), and on the right we show the one obtained with $R_A = 3$. We have not imposed the positivity constraint to the maps to allow an easier qualitative comparison. The smoothing of the discontinuities between annuli is quite evident when we take a larger optimization area, especially for the outer zones. So we take the map obtained for $R_A = 3$ as the best result; it is the one that we will use for the analysis.

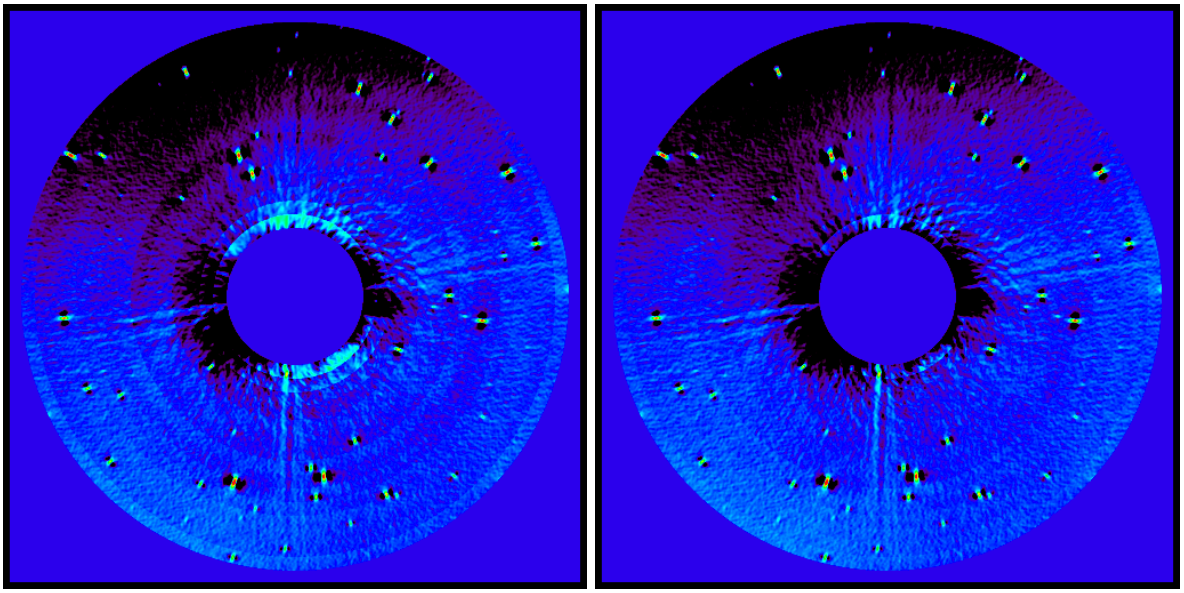

Figure 6. SNR map for the NACO target, obtained with $R_A = 1$ (left) and $R_A = 3$ (right) for the same annuli size. Positivity constraint is not applied.

At a glance, we can distinguish many detections from the typical radially elongated shape described in Subsect. 4.4.

The standard deviation of the SNR is higher than for the simulated images (8.67); this is probably due to a non optimal subtraction of the background which causes inhomogeneities in the images. For this reason we threshold the map at 2 (Fig. 7, left) instead of 3 like we did in Subsect. 4.4 and 4.5. We can recognize all the detections that we could spot by eye in the SNR map (Fig. 6, right). The right part of Fig. 7 shows the related flux map that we obtain. Once again, we can notice the different shape with respect to the SNR map (Fig. 6, right): in general, the minor peaks stand out less clearly in the flux map.

6. CONCLUSION

We recalled the principle of ANDROMEDA, an algorithm for exoplanet detection based on a maximum likelihood approach, and we presented the improvements made with respect to the previous version. In particular, we introduced the spectral diversity and the optimization of the differences in order to suppress the speckle more effectively. We showed the results of the validation of the algorithm both on simulated and experimental data. The simulations show that using the spectral diversity we can detect a companion 10^6 times fainter than the star at a separation of $4.9\lambda/D$. Although it has been developed in the context of IRDIS, in order to perform SDI and ADI, the method can also be applied to data taken by other instruments (for example in the context of polarimetric imaging).

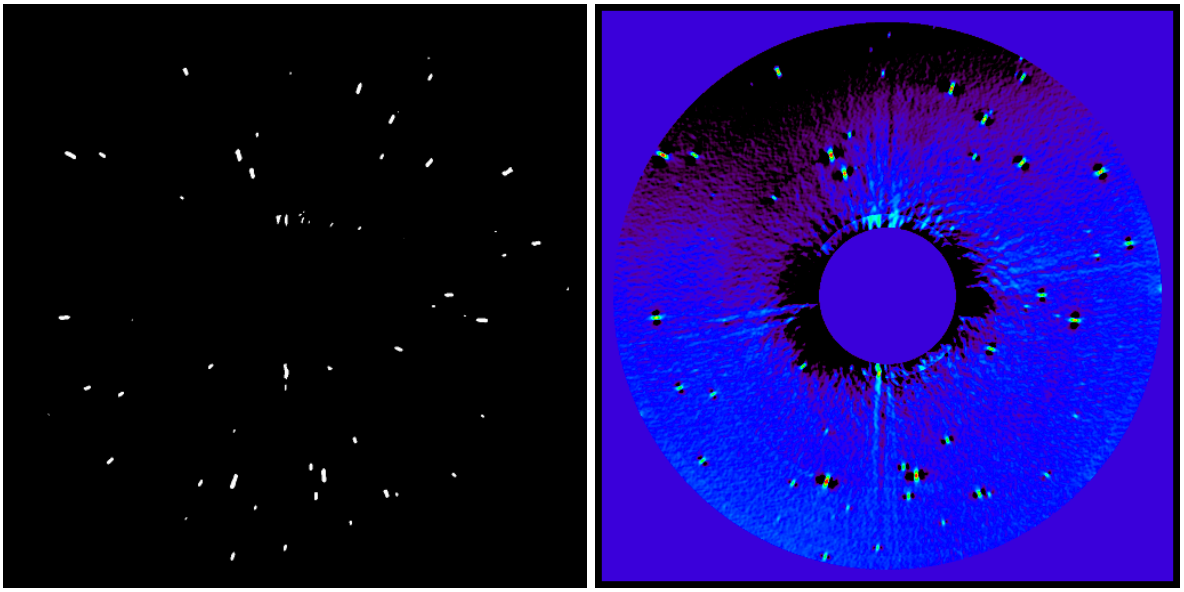

Figure 7. Normalized SNR map for the NACO target thresholded at 2 (left) and flux map for the NACO target (right).

Perspectives include refining the detection method to find the optimal thresholding strategy, as well as studying the optimal size of the subtraction annuli and the best value for the ratio between optimization area and subtraction area.

Furthermore, the method should be tested on coronagraphic experimental data (and not only on saturated images), and the results compared with those of other ADI-based methods. We also plan to characterize ANDROMEDA's performances at small separations by introducing artificial planets in NACO images.

Appendix A: Details on the wavelength rescaling algorithm

For conciseness we consider one-dimensional signals, and the results generalize readily to two dimensions. Given N samples of a signal i sampled with a pitch p_α, the quantity $\tilde{i}(kp_\nu)$ given by:

$$\tilde{i}(kp_\nu) = \sum_{l=0}^{N-1} i(lp_\alpha)\, e^{2j\pi\, lp_\alpha\, kp_\nu}, \tag{12}$$

is the DFT of i at frequency kp_ν, where p_ν is the pitch in Fourier space. Because of the use of the FFT, the pitch in Fourier and direct spaces are related by

$$p_\alpha p_\nu = 1/N, \tag{13}$$

which means that the support Np_α is the inverse of the Fourier pitch.

If we modify the number of pixels in direct space by adding on each side of the table some null pixels *before* performing the FFT, Eq. 13 becomes $p_\alpha p_{\nu'} = 1/N'$, where N' is the new signal size after zero-padding in direct space, and $p_{\nu'}$ the new pitch in Fourier space.

If we proceed similarly in Fourier space by adding null pixels after performing the FFT, we finally obtain for the new spatial sampling in direct space after an inverse FFT:

$$p_{\alpha''} = \frac{N'}{N''}\, p_\alpha, \tag{14}$$

where N'' is the new signal size after zero-padding in Fourier space. We have thus zoomed the image by a factor $z = (N''/N')$. Note that if we only zero-pad the image in Fourier space, as is often done, then $N' = N$, which severely constrains the zooming factor: $z = N''/N$.

In order to resample the coronagraphic star image at λ_2 according to Eq. 7, we need to satisfy the following equation:

$$\frac{N'}{N''} = \frac{\lambda_2}{\lambda_1}. \tag{15}$$

Having two degrees of freedom N' and N'' allows us, in practice, to satisfy this equality with a good precision (10^{-4} or so) for reasonable values of N' and N'' for all wavelengths of the IRDIS instrument.

ACKNOWLEDGMENTS

The authors would like to thank Markus Feldt and Christian Thalmann of the SPHERE consortium for fruitful discussions.

This research has been supported by Groupement d'Intérêt Scientifique PHASE (Partenariat Haute résolution Angulaire Sol Espace) between ONERA, Observatoire de Paris, CNRS and Université Paris Diderot, which is being extended to LAOG and LAM.

REFERENCES

[1] Beuzit, J.-L. et al., "SPHERE: a planet imager for the VLT," in [*Telescopes and Systems*], Proc. Soc. Photo-Opt. Instrum. Eng. (2010). Conference date: June 2010, San Diego.

[2] Fusco, T., Rousset, G., Sauvage, J.-F., Petit, C., Beuzit, J.-L., Dohlen, K., Mouillet, D., Charton, J., Nicolle, M., Kasper, M., and Puget, P., "High order adaptive optics requirements for direct detection of extra-solar planets. application to the sphere instrument.," *Opt. Express* **14**(17), 7515–7534 (2006).

[3] Rouan, D., Riaud, P., Boccaletti, A., Clénet, Y., and Labeyrie, A., "The Four-Quadrant Phase-Mask Coronagraph. I. Principle," *Pub. Astron. Soc. Pacific* **112**, 1479–1486 (Nov. 2000).

[4] Soummer, R., Aime, C., and Falloon, P. E., "Stellar coronagraphy with prolate apodized circular apertures," *Astron. Astrophys.* **397**, 1161–1172 (Jan. 2003).

[5] Boccaletti, A., Baudrand, J., Baudoz, P., and Riaud, P., "Development of Coronagraphs for Exoplanet Detection with SPHERE," in [*Proceedings of the conference In the Spirit of Bernard Lyot: The Direct Detection of Planets and Circumstellar Disks in the 21st Century. June 04 - 08, 2007. University of California, Berkeley, CA, USA. Edited by Paul Kalas.*], Kalas, P., ed. (June 2007).

[6] Racine, R., Walker, G. A., Nadeau, D., and Marois, C., "Speckle noise and the detection of faint companions," *Pub. Astron. Soc. Pacific* **112**, 587–594 (1999).

[7] Marois, C., Doyon, R., Nadeau, D., Racine, R., and Walker, G. A. H., "Effects of Quasi-Static Aberrations in Faint Companion Searches," in [*Astronomy with High Contrast Imaging*], Aime, C. and Soummer, R., eds., *EAS Publications Series* **8**, 233–243, EDP Sciences (2003).

[8] Labeyrie, A., "Detection of extra-solar planets," in [*Formation of Planetary Systems*], Brahic, A., ed., 883, 885–888, Cepadues-Editions, Toulouse (1982).

[9] Marois, C., Lafrenière, D., Doyon, R., Macintosh, B., and Nadeau, D., "Angular Differential Imaging: A Powerful High-Contrast Imaging Technique," *Astrophys. J.* **641**, 556–564 (Apr. 2006).

[10] Mugnier, L. M., Cornia, A., Sauvage, J.-F., Rousset, G., Fusco, T., and Védrenne, N., "Optimal method for exoplanet detection by angular differential imaging," *J. Opt. Soc. Am. A* **26**, 1326–1334 (June 2009).

[11] Lafrenière, D., Marois, C., Doyon, R., Nadeau, D., and Artigau, É., "A New Algorithm for Point-Spread Function Subtraction in High-Contrast Imaging: A Demonstration with Angular Differential Imaging," *Astrophys. J.* **660**, 770–780 (May 2007).

[12] Vigan, A., Moutou, C., Langlois, M., Allard, F., Boccaletti, A., Carbillet, M., Mouillet, D., and Smith, I., "Photometric exoplanet characterization with angular and spectral differential imaging," *ArXiv e-prints* (Apr. 2010). Accepted for publication in MNRAS.

[13] Vigan, A., Moutou, C., Langlois, M., Mouillet, D., Dohlen, K., Boccaletti, A., Carbillet, M., Smith, I., Ferrari, A., Mugnier, L., and Thalmann, C., "Comparison of methods for detection and characterization of exoplanets with SPHERE/IRDIS," in [*Telescopes and Systems*], Proc. Soc. Photo-Opt. Instrum. Eng. (2010). Conference date: June 2010, San Diego.